Available online at www.sciencedirect.com

jmr&t Journal of Materials Research and Technology

journal homepage: www.elsevier.com/locate/jmrt

Original Article

Long-term high-temperature behavior of Ti–Al based electrodes for surface acoustic wave devices

*Marietta Seifert**, *Barbara Leszczynska*, *Siegfried Menzel*, *Thomas Gemming*

Leibniz IFW Dresden, Helmholtzstr. 20, 01069 Dresden, Germany

ARTICLE INFO

Article history:
Received 24 January 2022
Accepted 4 April 2022
Available online 13 May 2022

Keywords:
High-temperature
Surface acoustic wave device
Sensor
TiAl electrodes
CTGS

ABSTRACT

The long-term high-temperature behavior of Ti–Al based electrodes for the application in surface acoustic wave (SAW) sensor devices was analyzed. The electrodes were obtained by e-beam evaporation of Ti/Al multilayers on the high-temperature stable piezoelectric $Ca_3TaGa_3Si_2O_{14}$ (CTGS) substrates and structuring via the lift-off process. AlNO (25 at.% Al; 60 at.% N and 15 at.% O) cover and barrier layers were applied as protection against oxidation from the surrounding atmosphere and to prohibit a chemical reaction with the substrate. The samples were annealed at temperatures up to 600 °C in air for a duration of up to 192 h. Scanning and transmission electron microscopy were used to evaluate the morphology and degradation of the electrodes as well as of the extended contact pads. The results revealed that the Ti–Al based electrodes remained unoxidized after annealing for 192 h at 400 and 500 °C and for 24 h at 600 °C. After the heat treatment for 192 h at 600 °C, a strong oxidation of the structured electrodes occurred, which was less pronounced within the pads. In summary, the investigation showed that Ti–Al based SAW devices are a cost efficient alternative for long-term applications up to at least 500 °C and short- and medium-term applications up to 600 °C.

1. Introduction

Sensors working at high temperatures above 350 °C have attracted much attention for a wide range of industrial applications [1–3]. The knowledge of physical parameters as temperature or pressure is a key requirement to control and optimize high-temperature processes. Sensors working on the principle of surface acoustic waves (SAW) combine the advantages of a passive operation and wireless interrogation and therefore allow the measurement of physical parameters at components, e.g. turbine blades, which cannot be accessed by wired devices due to their position or movements [2–5].

The key part of a SAW sensor is the so called interdigital transducer (IDT), a structure comprising an entangled pair of comb-like electrodes on a piezoelectric substrate. By application of a high-frequency voltage surface acoustic waves are generated via the inverse piezoelectric effect. The high-frequency signal can be transferred by an antenna. One way to electrically connect the antenna and the IDT is the wire bonding from the antenna to a bond pad, which is connected to the IDT structure.

* Corresponding author.
E-mail address: marietta.seifert@ifw-dresden.de (M. Seifert).

https://doi.org/10.1016/j.jmrt.2022.04.027

During the last years, there have been a lot of efforts by several groups to develop, investigate and improve high-temperature stable metallizations and oxidation barrier systems which can be used to realize SAW devices that can operate at high temperatures. Among these materials, the focus has been mainly on noble metals such as Pt [6–10] or Pt-Rh [11], Pd [12], and Ir [13,14] or Ir-Rh [15] as well as refractory metals like W and Mo [16,17].

In literature, for Pt-based sensors a long-term high-temperature stability was shown up to 800 °C for a few months [18]. A short term stability of at least 60 min up to 1100 °C or even 1300 °C was also demonstrated [10]. However, electrode structures of noble metals tend to agglomerate or oxidize at very high temperatures. In addition, due to their high costs, such materials are not attractive for industrial mass production.

Up to now, non-noble metals like Al, Ti and Cu with their low melting temperatures and low costs have been reported as metallization for SAW devices, which provide a high power durability at room temperature (RT) or only slightly elevated temperatures (mainly <100 °C) [2,19–24]. However, there are Al-based alloys which possess significantly higher melting temperatures and a sufficient oxidation resistance, making them interesting candidates to realize SAW devices applicable at high-temperatures. In former years, we investigated the promising intermetallic Al based alloys TiAl [25,26] and RuAl [27,28] regarding their suitability for application in high-temperature SAW devices. In contrast to the noble materials, these alloys are much cheaper, which is an important factor for an industrial application.

In our former work we demonstrated that TiAl thin films, which were deposited as Ti/Al multilayer stacks on high-temperature stable $Ca_3TaGa_3Si_2O_{14}$ (CTGS) substrates, promise an applicability in an intermediate temperature regime of up to 600 °C in air using cover and barrier layers composed of 25 at.% aluminum, 60 at.% nitrogen and 15 at.% oxygen (AlNO) [26]. The deposition of TiAl multilayers and a subsequent annealing was chosen to obtain the TiAl phase since the deposition of a Ti–Al alloy and subsequent annealing did not result in the formation of a TiAl phase [25]. However, these investigations were restricted to extended films and therefore could not resolve the still open question of the additional effects taking place at the edges of structured electrodes. Owing to the limited width of the fingers (about 1.5 μm) and possible variations of the residual stress due to the structuring, changes in the microstructure as compared to the extended films might occur. In addition, it had to be investigated to what extent the edges of the fingers and their coatings might be starting points for further oxidation processes.

The present paper reports on a detailed investigation of the grain structure and degradation of TiAl IDTs by transmission electron microscopy of the cross sections of the fingers. To reveal the influence of the limited size and edges of the fingers, cross sections of the extended bond pads with a size of several 100 μm were analyzed as well.

2. Experimental section

The electrodes were produced by deposition of Ti/Al multilayer films and subsequent structuring via the lift-off technique. In the first step, the lift-off mask for the structuring of the IDTs was prepared on the CTGS substrate. Subsequently, a 20 nm thick AlNO barrier layer was deposited by magnetron sputtering from an AlN target using a mixture of 40 sccm: 8 sccm of Ar and N_2 as the sputtering gas. According to energy dispersive X-ray spectroscopy in the transmission electron microscope, these layers had a composition of about 60 at.% N, 15 at.% O and 25 at.% Al in the as-prepared state. Then, the Ti/Al multilayer was deposited by e-beam evaporation with an individual layer thickness of 10 nm, starting with Ti, and a total thickness of 200 nm, with Al as the uppermost layer. The metallic targets were supplied by J. Lesker Company with a purity of 99.8. Details of the deposition of the Ti/Al layers were described in [26]. In the next step, the lift-off procedure was carried out by removing the lift-off mask using suited solvents. As a final step, 40 nm of AlNO were added as a cover layer which, as a consequence, then also covered the bare CTGS substrate in-between the fingers and individual electrode structures. A one-port resonator structure was used as the SAW device layout. An overview image demonstrating the location of the fingers and contact pads is shown in Fig. 1. Devices with a varying width of the fingers between 1.4 and 2 μm were used for this annealing study.

To prove the suitability of the TiAl-based devices, Fig. 1b shows the electrical characteristics of a SAW resonator. The characterization of the electrical behavior was carried out via electrical *S*-parameter measurements with a vector network analyzer (VNA, Keysight E5080B).

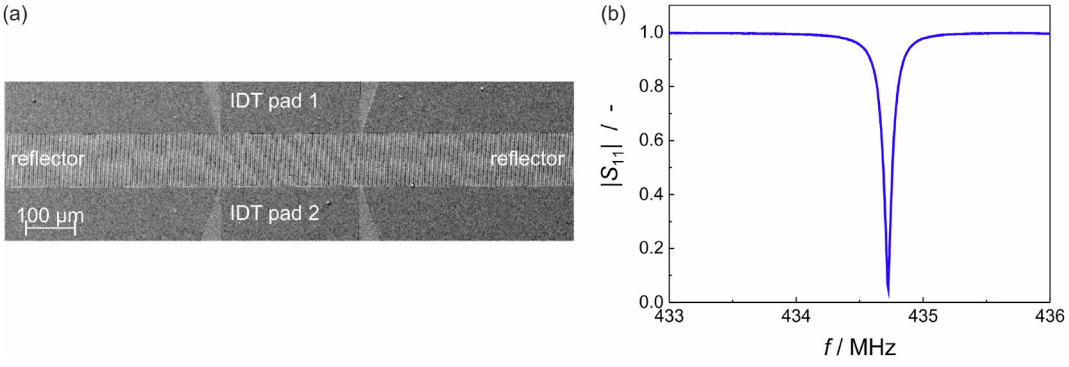

Fig. 1 – (a) SEM image (SE, 5 kV) of the SAW device layout, (b) Electrical characteristics in terms of the reflection coefficient $\|S_{11}\|$ of a one-port resonator structure with TiAl metallization after an annealing at 600 °C in UHV for 10 h.

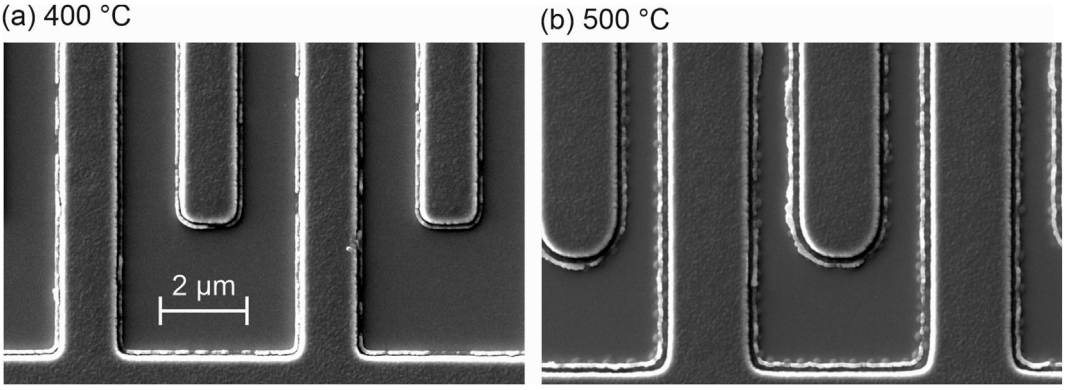

Fig. 2 – SEM images of the IDT electrodes after annealing in air for 192 h at (a) 400 °C (width of the fingers: 1.4 µm) and (b) 500 °C (width of the fingers: 2 µm).

The frequency dependent input reflection coefficient $\|S_{11}\|$ shows a resonant behavior. The relation of wavelength and frequency is given by $v = \lambda \cdot f$, whereby the wavelength λ of the SAW is choosen by the periodicity of the electrodes inside the resonator, whereas the phase velocity v depends mainly on the substrate material and propagation orientation and slightly on the electrode metallization. Figure 1b shows the characteristic resonance peak of $\|S_{11}\|$. The very low value of the electrical reflection indicated good impedance matching, i.e., there was almost no reflection of the electric energy from the device towards the signal generator. If there were equal characteristic impedances of the SAW device and the generator, the reflection would completely vanish to $\|S_{11}\| = 0$.

The samples were annealed in a tube furnace (glass tube) in air at 400 and 500 °C for 192 h and at 600 °C for 24, 48, 96 and 192 h.

Scanning electron microscopy (SEM, Helios 5 CX, Thermo Fisher Scientific, Waltham, MA, USA) was used to image the IDTs with an ICE detector at 5 kV acceleration voltage. Conventional and scanning transmission electron microscopy (TEM/STEM, Technai F30, FEI company, Hillsboro, OR, USA) of lamellas prepared by the focussed ion beam technique (FIB, Helios 5 CX, Thermo fisher scientific, Waltham, MA, USA) were applied to investigate the grain structure and to reveal possible degradation. The local composition and chemical bonding were determined by energy dispersive X-ray spectroscopy (EDX, Octane T Optima, EDAX Company, Mahwah, NJ, USA) and electron energy loss spectroscopy (EELS, GIF 200, Gatan, CA USA) in the TEM.

3. Results

3.1. *Annealing at 400 and 500 °C in air*

In the first experiments, the samples were annealed at 400 and 500 °C in air for 192 h. Figure 2 shows SEM images of the finger electrode structures after the annealing. Defects were visible neither in the fingers nor in the contact pads. However, parallel to the contour of the fingers, there were bright narrow features.

STEM images of the edges of the fingers and of a region within the contact pads are summarized in Fig. 3. In addition, overview

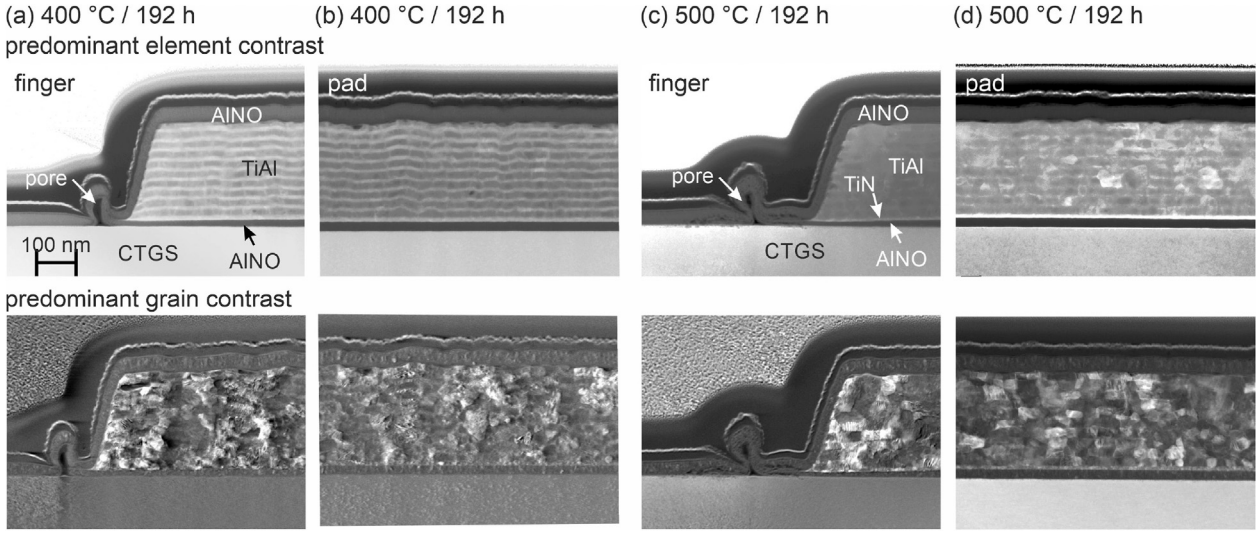

Fig. 3 – STEM images of the electrode metallization annealed for 192 h in air: (a) finger and (b) contact pad at 400 °C, (c) finger and (d) contact pad at 500 °C. The top images show predominant element contrast, the lower images show predominant grain contrast.

STEM images of the cross sections of the fingers and contact pads are summarized in the Appendix in Fig. A1 and Fig. A2.

In the images of the sample annealed at 400 °C it can be seen that the interdiffusion between the Al and Ti layers was not completed at this low temperature. A sequence of brighter and darker layers was visible (Fig. 3a and b, upper part). EDX measurements revealed that the bright layers had a composition of about 67 at.% Ti and 33 at.% Al, which according to the TiAl phase diagram corresponds to the Ti_3Al phase [29]. The dark layers had a composition of about 66 at.% Al and 34 at.% Ti, which corresponds to the $TiAl_2$ phase.

In contrast to this, the annealing at 500 °C led to a much stronger interdiffusion of the Ti and Al layers and only a weak contrast was visible in the images with elemental contrast (3c and d upper part). There was still a layer structure, as can be also seen from the grain boundaries parallel to the film plane (3c and d lower part). The grains were larger and appeared more uniform as compared to the sample annealed at 400 °C (3a and b lower part). The EDX measurements showed that the brighter layers had a composition of 57 at.% of Al and 43 at.% of Ti, which corresponds to the composition of TiAl. The existence range of TiAl according to the phase diagram is 55–58 at% Al at 500 °C [29]. The composition of the darker layers in-between was about 63 at.% of Al and 37 at.% of Ti, which is close to $TiAl_2$. For both temperatures, no difference in the elemental distribution or grain contrast was visible between the fingers and the contact pad.

The annealing at 400 °C did not lead to a degradation of the AlNO cover layer. The heat treatment at 500 °C led to a slight oxidation of the uppermost few nm of the AlNO, which was visible in STEM images with a higher magnification as a dark contrast at the surface of the AlNO.

At both sides of the fingers, the STEM images showed loop-like features, which enclosed pores. These structures led to the bright contrast next to the electrode fingers, which was visible in the SEM images in Fig. 2. A possible explanation of the origin will be discussed below.

3.2. *Annealing at 600 °C in air*

Figure 4 summarizes the SEM images of the electrodes after the different annealings at 600 °C in air.

After annealing for 24 h, no obvious defects were visible. The annealing for 48 h led to the formation of large bubbles in-between the fingers. In addition, the roughness of the fingers increased. Locally, small (few nm) bright structures appeared. They were distributed inhomogeneously at the fingers and contact pads. There were also regions without such structures. With increasing the annealing duration, these small structures increased in size and density. The surface of the fingers and pads became rougher. Interestingly, the big bubbles present after annealing for 48 h in-between the fingers were not detected for the longer annealing times, for which only small bubbles were found. For all samples, as for the annealings at lower temperatures, bright structures appeared around the fingers.

Long hair-like bright objects were found on some of the samples. These were most likely residuals of the lift-off mask, which were not completely removed by the solvent and remained attached to the surface. However, this issue is not crucial for laboratory investigations and is prevented in industrial routines.

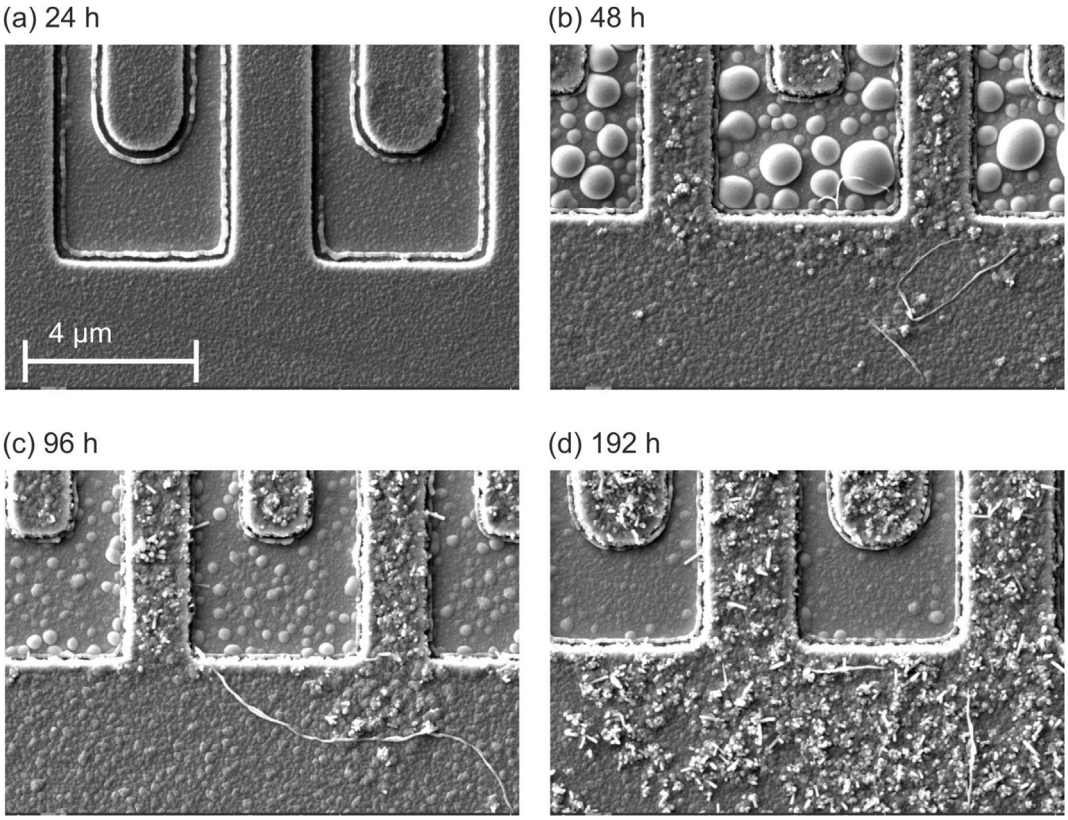

Fig. 4 – SEM images of the IDTs after annealing at 600 °C in air for (a) 24 h, (b) 48 h, (c) 96 h, and (d) 192 h.

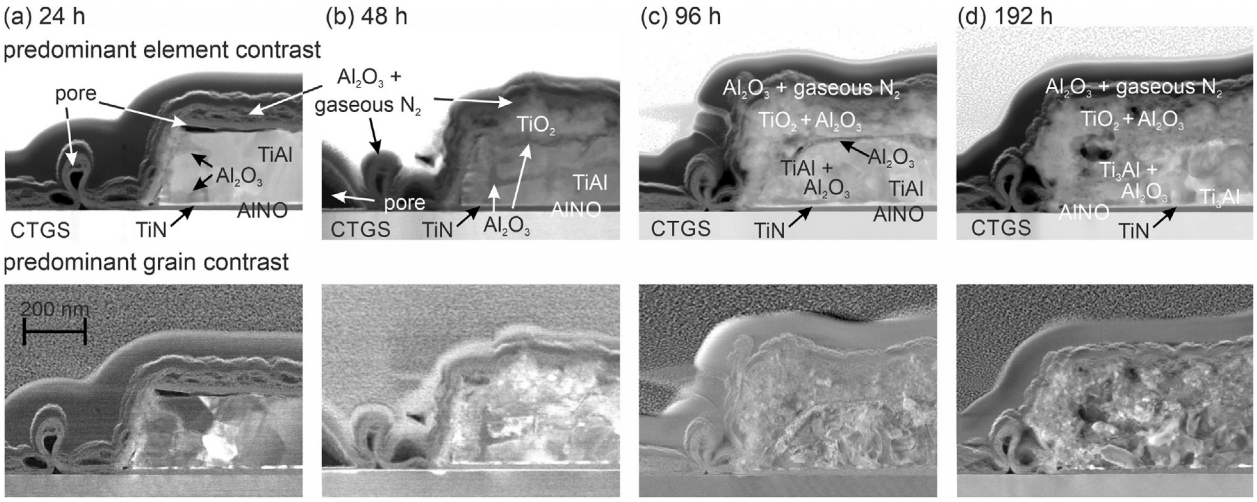

Fig. 5 – STEM images of the IDT fingers annealed for (a) 24 h, (b) 48 h, (c) 96 h, and (d) 192 h at 600 °C in air. The top images show predominant element contrast, the lower images show predominant grain contrast.

Figure 5 shows a comparison of the STEM images of edges of the IDT fingers and Fig. 6 of a region of the contact pad after the different annealing times at 600 °C in air. A complete set of overview STEM images of the cross sections of the IDT fingers and of the pads is summarized in the Appendix in Figs. A3–A6.

3.2.1. *Annealing for 24 h*

The STEM images of a finger structure and a pad of the sample annealed for 24 h at 600 °C are shown in Figs. 5a and 6a, respectively. Overview images are presented in the Appendix in Fig. A3. The measurements revealed that there was hardly any degradation after this heat treatment. The finger as well as the pad possessed a homogeneous element distribution. In contrast to the annealing procedures at lower temperatures, no layered structure was visible anymore in the images with element contrast. There was only a slight oxidation and formation of very few Al_2O_3 grains near to the edges of the finger (darker regions visible at the edge of the finger, Fig. 5a upper part). The composition of the AlNO barrier layer between the metallization and the substrate remained unchanged. In contrast to this, the former AlNO cover layer was degraded. It increased in thickness to approximately 70 nm, consisting then of a lower, more dense region and an upper region, which contained a lot of small pores. EDX and EELS measurements showed that the heat treatment led to an oxidation of this layer. It then consisted of Al_2O_3 and N which, according to the EELS signal, was not bound to Al–O anymore but instead was present as N_2. It is assumed that during the oxidation of the AlNO N_2 was emitted, which led to the formation of the pores visible in the upper region of the cover layer.

The grain structure of the finger and the pad was comparable and inhomogeneous (Figs. 5a and 6a). There were a few large grains, which were extended across the whole sample thickness (see also overview image Fig. A3). However, the majority of the grains was much smaller with a size of some tens of nm.

At the interface between the AlNO barrier layer and the TiAl metallization, the known chemical reaction between Ti and AlN led to the formation of a thin TiN layer, as described in [26]. This layer was visible as a thin bright line directly above the AlNO layer in both images with the different contrast.

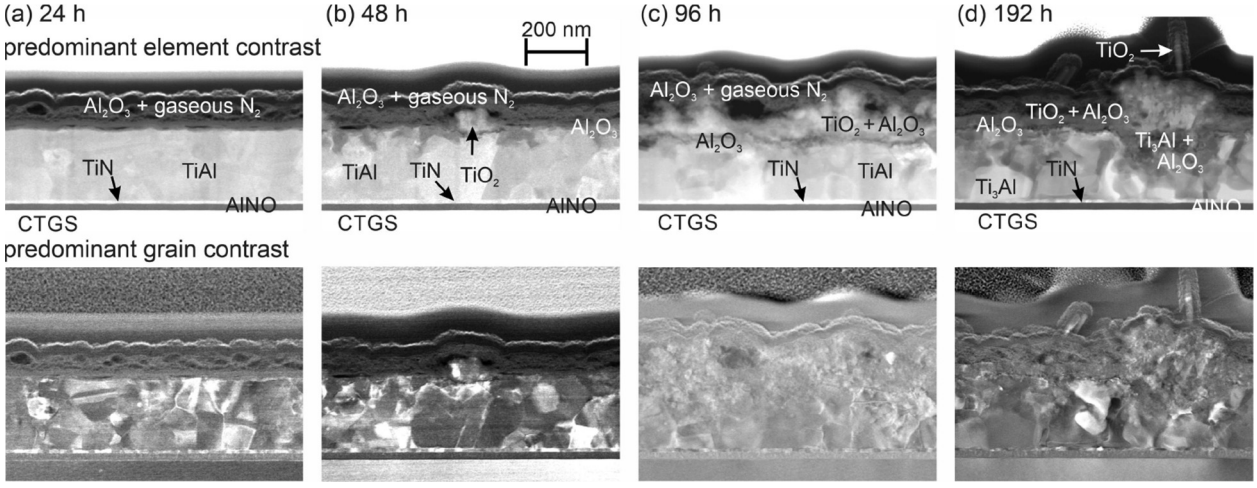

Fig. 6 – STEM images of the contact pads of the samples annealed for (a) 24 h, (b) 48 h, (c) 96 h, and (d) 192 h at 600 °C in air. The top images show predominant element contrast, the lower images show predominant grain contrast.

3.2.2. *Annealing for 48 h*

In Figs. 5b and 6b, the STEM images of the sample annealed for 48 h at 600 °C are summarized. Overview images are shown in the Appendix in Fig. A4. The results demonstrated that there was an increased degradation and that the surface roughness increased as compared to the annealing for 24 h.

In the image with predominant element contrast, the original shape of the finger was still visible since it was surrounded by a dark thin layer (Fig. A4a). EDX measurements revealed that at the surface of the metallic material a thin Al_2O_3 layer has formed, which led to the dark contrast.

The composition of the finger itself remained almost homogeneous with a small amount of Al_2O_3 at the edges of the fingers and a few Al_2O_3 grains in the upper part of the metallization (Fig. 5b upper part). There was a slight change in the grain structure. There were some larger grains in the center of the finger, while close to the edges the grain structure appeared more inhomogeneous with mainly smaller grains (Fig. 5b lower part).

In contrast to the sample annealed for 24 h, in which only a minor oxidation of Al took place, the annealing for 48 h in addition led to a partly oxidation of Ti. TiO_2 was detected outside of the original finger structure with a varying thickness, causing the brighter structures visible the STEM and SEM images. In summary, the degraded layer on top of the metallization consisted of a thin layer of Al_2O_3, followed by an about 90–120 nm thick layer of a mixture of TiO_2 and Al_2O_3 in the lower part and above a porous layer of Al_2O_3 with pores filled with N_2.

The SEM image in Fig. 4 showed large bubbles in-between the finger electrodes. The STEM images proved that there almost the whole barrier layer was lifted off the substrate. However, a very thin layer of Al_2O_3 with N_2 with a thickness of only a few nm remained at the surface of the CTGS. It is assumed that a chemical reaction between the O of the substrate and the deposited AlNO led to a thin layer, which remained attached to the CTGS. The origin of the formation of the large bubbles is still unclear. As observed for the sample annealed for 24 h, loop-like structures were present at both sides of the fingers.

The STEM images of the contact pad (Fig. 6b and Fig. A4b) showed a difference of the degraded layer on top. Its thickness was smaller as compared to the finger (60–70 nm). It consisted of Al_2O_3 with N_2. Only locally TiO_2 grains were formed between the metallic layer and the cover. There was no continuous layer of TiO_2 and Al_2O_3 as observed for the finger electrode. However, as for the finger, some Al_2O_3 was also detected in the uppermost part of the metallic layer. The grain structure appeared different to that of the finger. There was a mixture of smaller and bigger grains, which were distributed more homogeneously.

3.2.3. *Annealing for 96 h*

STEM images of the electrodes and contact pad of the sample annealed for 96 h in air at 600 °C are summarized in Figs. 5c and 6c. Overview images are shown in the Appendix in Fig. A5.

The original shape of the finger was still identifiable (Fig. A5a). As observed for the sample annealed for 48 h, a thin dark layer consisting of Al_2O_3 separated the metallic material from the oxide layer on top (Fig. A5a upper part). The thickness of the degraded layer further increased and was between 120 and 200 nm for the finger electrode. It mainly consisted of TiO_2 with some Al_2O_3. At the surface, the residue of the original cover layer was present in form of Al_2O_3 with N_2. The roughness further increased as compared to the shorter annealing time.

Inside the finger, TiAl was still present. However, the content of Al_2O_3 had increased and was not restricted anymore to the edges and the uppermost region of the metallization (Fig. A5a upper part). In the image with predominant grain contrast, a few larger grains were visible in the center of the finger (Fig. A5a lower part). The rest of the grain structure appeared inhomogeneous with small grains. The loop-like structures at the sides of the electrodes were also still present.

As observed for the shorter annealing time, the degraded zone on top of the pad was thinner with a thickness of 120–160 nm and its roughness was lower as compared to the finger (Fig. 5b). While after annealing for 48 h TiO_2 grains were present only locally, there was a continuous layer of TiO_2 with some Al_2O_3. As observed for the finger, the uppermost layer was Al_2O_3 with N_2. Al_2O_3 was formed in the metallic layer only at few positions. The grain structure of the contact pad consisted of larger grains as compared to the finger.

3.2.4. *Annealing for 192 h*

Figs. 5d and 6d summarize the STEM images of the sample annealed at 600 °C in air for 192 h. Overview images are shown in the Appendix in Fig. A6. In contrast to the IDTs annealed for shorter times, it was not possible anymore to identify the original shape of the finger (Fig. A6). There was a very inhomogeneous distribution of the elements and shape of the grains. There were a few brighter grains in the lower part of the sample visible in the image with predominant element contrast, which appeared homogeneous in the image with predominant grain contrast. EDX measurements revealed that they were composed of Ti_3Al. Above these grains, there was a mixture of Ti_3Al and Al_2O_3. The strong oxidation of Al led to a lack of Al for the formation of the TiAl phase, so that the Ti-rich Ti_3Al was formed. The measured composition of about 70 at.% of Ti and 30 at.% of Al is within the existence range of the Ti_3Al phase, which is between about 61 and 83 at.% Ti at 600 °C according to the Ti–Al phase diagram [29].

On top of the contact pad, locally big TiO_2 grains have formed. As observed for the finger, the pad also consisted of a mixture of Ti_3Al and Al_2O_3 (Fig. A6b). However, the grain structure appeared more homogeneous as compared to the finger.

Locally, small sharp features were visible at the sample surface, as e.g., in Fig. A6b in the STEM image of the pad. EDX measurements showed that these needle-like structures consisted of TiO_2. These features were also visible in the SEM image in Fig. 4d, where they led to a bright contrast.

4. Discussion

The oxidation processes in Ti–Al materials were discussed extensively in literature (e.g. [30–32]). It is known that due to differences in the diffusion velocities of the involved elements, the growth of TiO_2 is directed outwards of the sample. In contrast, the growth direction of Al_2O_3 points inwards. The distribution of Al_2O_3 and TiO_2 in the samples after the annealings at 600 °C corresponded with this theory. TiO_2 was only found outside of the initial region of the TiAl

metallization, while Al_2O_3 was mainly present at the interface between the initial TiAl metallization and the AlNO cover layer as well as inside the initial TiAl metallization. The formation of Ti_3Al after the annealing at 600 °C in air for 192 h showed that the oxidation of Al was faster than that of Ti. More Al was oxidized, leading to a Ti-rich Ti–Al phase.

Our investigations demonstrated that after annealing at 400 °C for 192 h, the AlNO cover layer did not degrade at all. After the annealing at 500 °C for 192 h, there was only a very minor oxidation of the uppermost layer of the AlNO. However, already after annealing for 24 h at 600 °C, the AlNO cover layer was degraded. Al_2O_3 was formed, in which bubbles of N_2 were embedded. For all annealing durations at 600 °C, such an Al_2O_3–N_2 layer was found on top of the sample. In addition, the cross sections revealed that the edges of the fingers acted as starting points for the diffusion of O inside the finger. After annealing for 24 h at 600 °C, a small amount of Al_2O_3 was found near to the edges. With increasing annealing time, this amount increased as well. It is assumed that the reason for this oxidation was the reduced thickness of the protection layer at the inclined edges of the finger. At these positions, the cover layer thickness was only a few nm in contrast to the 40 nm thick AlNO layer on top of the fingers and pads. This thin layer obviously did not sufficiently act as a diffusion barrier. The comparison of the behavior of the pads and IDT fingers also demonstrated the increased degradation of the fingers as compared to the pads. The pads contained less oxides as compared to the fingers, and also the roughness and thickness were smaller, as can be seen in the overview images in Figs. A3–A6.

For all annealings, an almost similar loop-like structure of the AlNO layer was observed at the edges of the fingers. Cross sections of fingers in the as-prepared state showed small structures at the sides of the fingers, which were extended perpendicular to the substrate, as can be seen in Fig. 7. EDX measurements revealed that they consisted of Al_2O_3. As described above, the structuring was done using the lift-off technique, which means that at first the lift-off mask was structured on the substrate. Then, the AlNO barrier layer was deposited via magnetron sputtering. Since the sputtering led to a wide distribution of directions of the deposited particles, also a part of the side edges of the lift-off mask was covered. The decreased thickness of the AlNO barrier layer in the center of the fingers as compared to their edges visible in the overview STEM images was also a consequence of the deposition via sputtering, which led to a reduced amount of material deposited close to the edges of the lift-off mask. The subsequent metallic layers were prepared via e-beam deposition, which was more directed, so that no deposition of the sides of the lift-off mask occurred. After the removal of the lift-off mask, a small rest of material remained there.

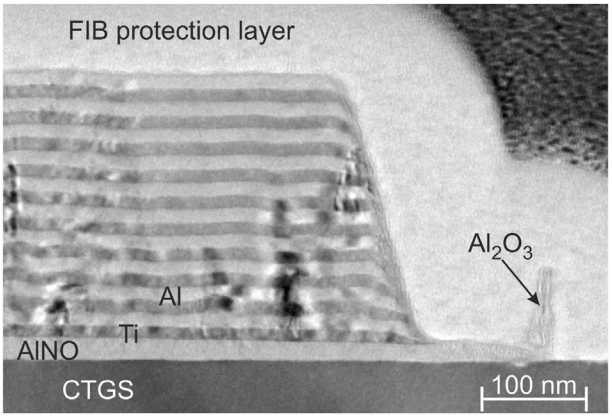

Fig. 7 – TEM image of an IDT finger in the as-prepared state.

The distance between the Al_2O_3-"edge" visible in Fig. 7 and the finger itself fitted well with the distance between the loop-like structures and the fingers in the STEM images. Therefore, it is assumed that this residual caused the loop-structures. After the lift-off procedure, the AlNO cover layer was deposited on the sample. Due to the sputtering, an AlNO layer was also deposited on both sides of the edge, leading to the loop structure. Therefore, in addition, in the region between the finger and the loop in the annealed samples, it appeared that the cover layer consisted of an upper and a lower part (see Fig. 5a-d), i.e., the AlNO barrier and cover layer, while outside of the loop, only the AlNO cover layer was present.

5. Conclusions

This paper presents a detailed TEM investigation of TiAl based IDT electrode structures and contact pads for use in surface acoustic wave devices after performing long-time annealings in air between 400 and 600 °C.

The results revealed that after annealing at 400 and 500 °C for 192 h, no degradation of the electrodes or the contact pads occurred. The annealing temperature of 400 °C was to low to realize a homogeneous microstructure by interdiffusion of the Ti/Al multilayers. A layered architecture consisting of Ti_3Al and $TiAl_2$ was formed. The interdiffusion was improved after annealing at 500 °C. However, there was still a multilayer structure with TiAl and $TiAl_2$.

After the heat treatment at 600 °C in air for 24 h, there was hardly any degradation. However, after annealing for 48 h, the formation of Al_2O_3 within the finger and TiO_2 on top of the metallization was detected. With increasing annealing time, the oxidation of Al mainly within the initial metallic layer and the formation of TiO_2 on top of the finger strongly increased. For all annealing durations, the degradation of the metallization of the finger was stronger as compared to the contact pad. These results proved that the edges of the fingers, where the cover layer has a reduced thickness due to the deposition from top, served as starting points for oxygen diffusion into the sample.

In summary, we can conclude that the TiAl based SAW sensors are promising cost efficient alternatives to noble-metal based devices for long-term application up to at least 500 °C and short- and medium-term application up to 600 °C. Prior to application, a pre-annealing of the devices at 600 °C in HV has to be performed to realize a full interdiffusion of the Ti and Al layers.

Data availability

The raw/processed data required to reproduce these findings can be shared upon reasonable request.

Declaration of Competing Interest

The authors declare that they have no known competing financial interests or personal relationships that could have appeared to influence the work reported in this paper.

Acknowledgements

The work was supported by German BMWI (03ET1589 A).

The authors gratefully acknowledge Hagen Schmidt for providing the layouts for the SAW resonators.

The authors gratefully acknowledge Andreas Büst for the deposition of the films as well as Thomas Wiek and Dina Bieberstein for SEM images and TEM lamella preparation.

The open access publication of this article was partly funded by the Open Access Fund of the Leibniz Association.

Appendix A. Overview STEM images

Figures A.1 and A.2 summarize overview STEM images of the IDT fingers and pads of the samples annealed at 400 °C and 500 °C in air for 192 h.

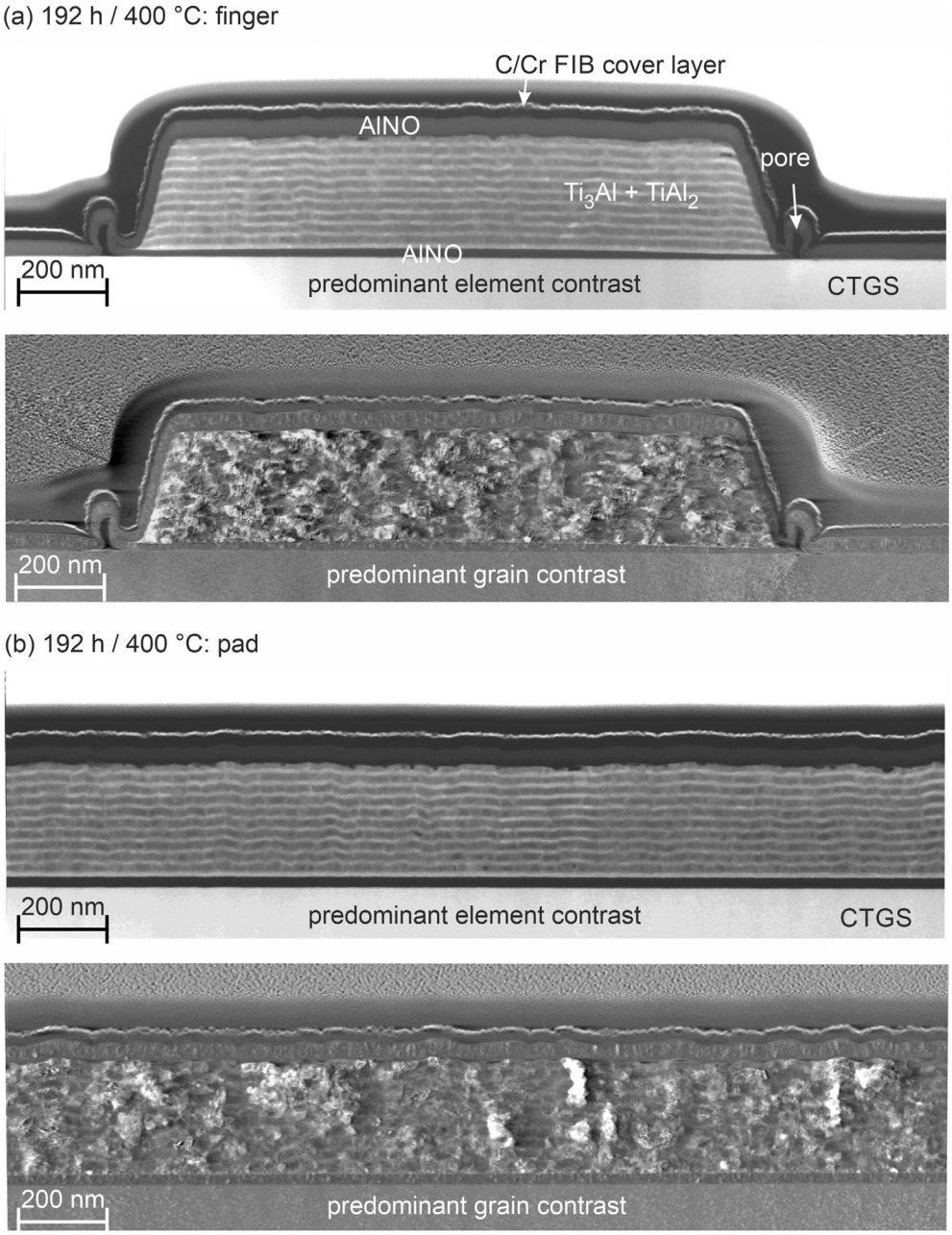

Figure A.1 – STEM images of the sample annealed for 192 h at 400 °C: (a) cross section of a finger electrode, (b) cross section of the contact pad. The top image shows predominant element contrast, the lower image shows predominant grain contrast.

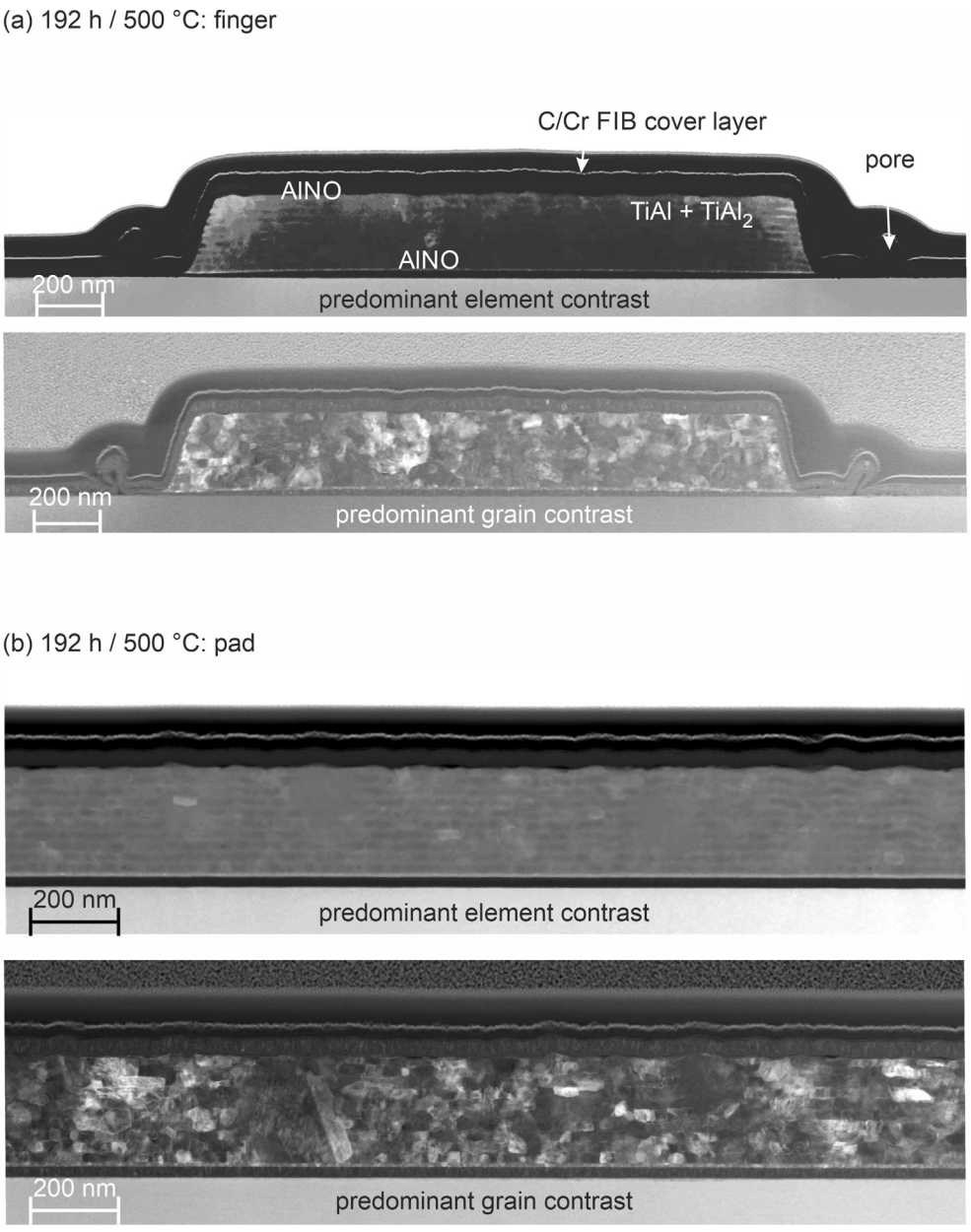

Figure A.2 – STEM images of the sample annealed for 192 h at 500 °C: (a) cross section of a finger electrode, (b) cross section of the contact pad. The top image shows predominant element contrast, the lower image shows predominant grain contrast.

Figures A.3–A.6 summarize overview STEM images of the IDT fingers and pads of the samples annealed at 600 °C in air for the annealing times between 24 h and 192 h.

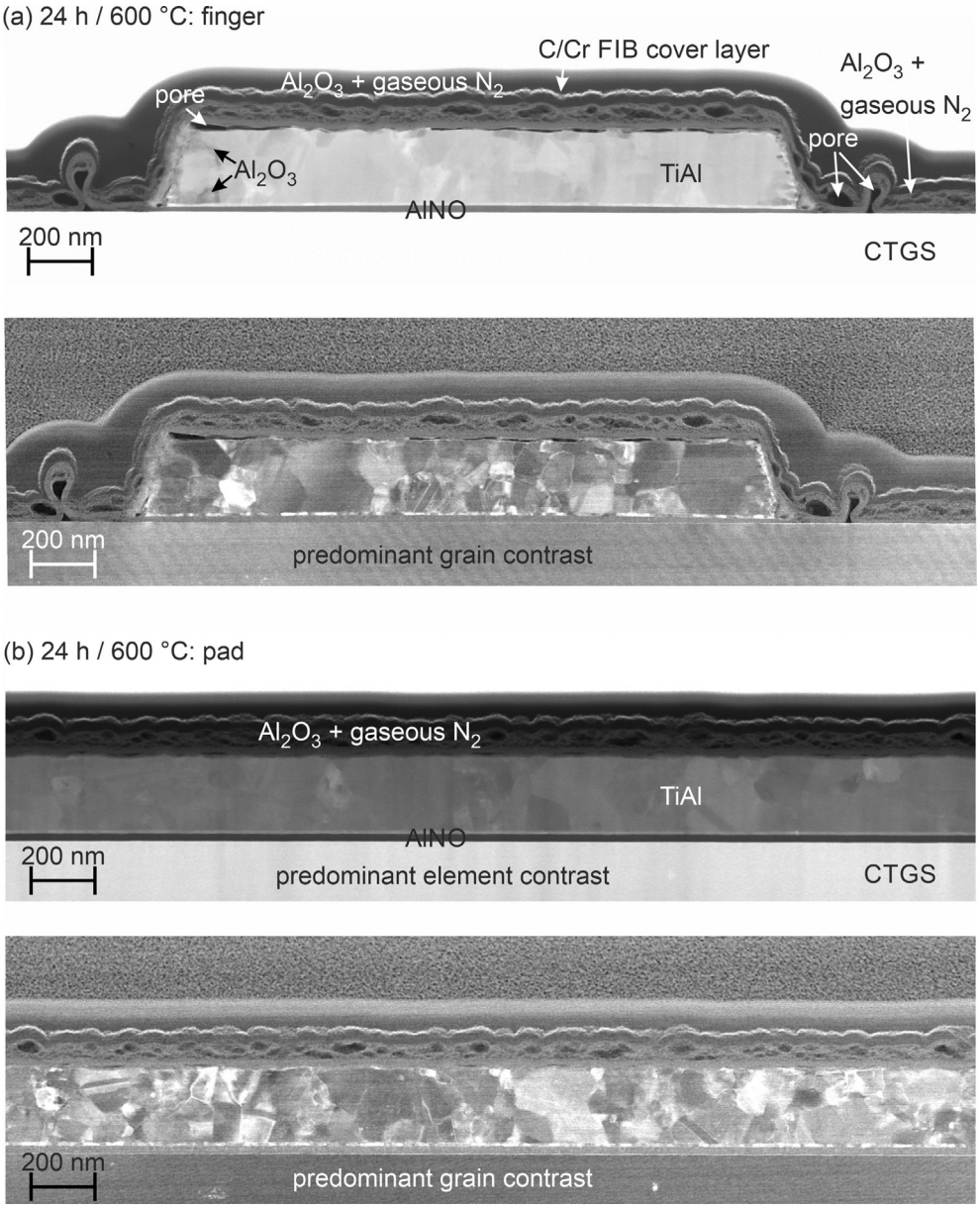

Figure A.3 – STEM images of the sample annealed for 24 h at 600 °C: (a) cross section of a finger electrode, (b) cross section of the contact pad. The top image shows predominant element contrast, the lower image shows predominant grain contrast.

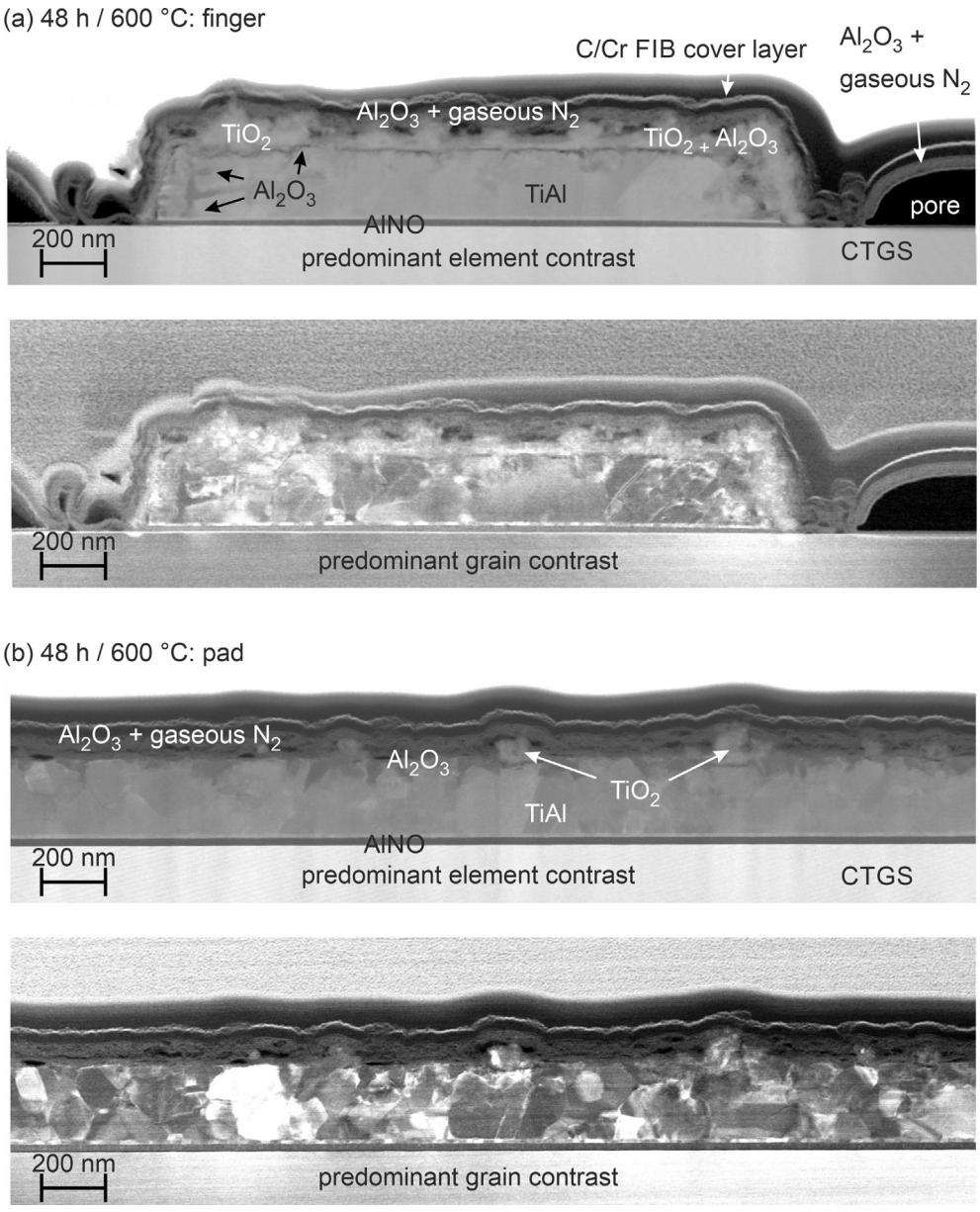

Figure A.4 – STEM images of the sample annealed for 48 h at 600 °C: (a) cross section of a finger electrode, (b) cross section of the contact pad. The top image shows predominant element contrast, the lower image shows predominant grain contrast.

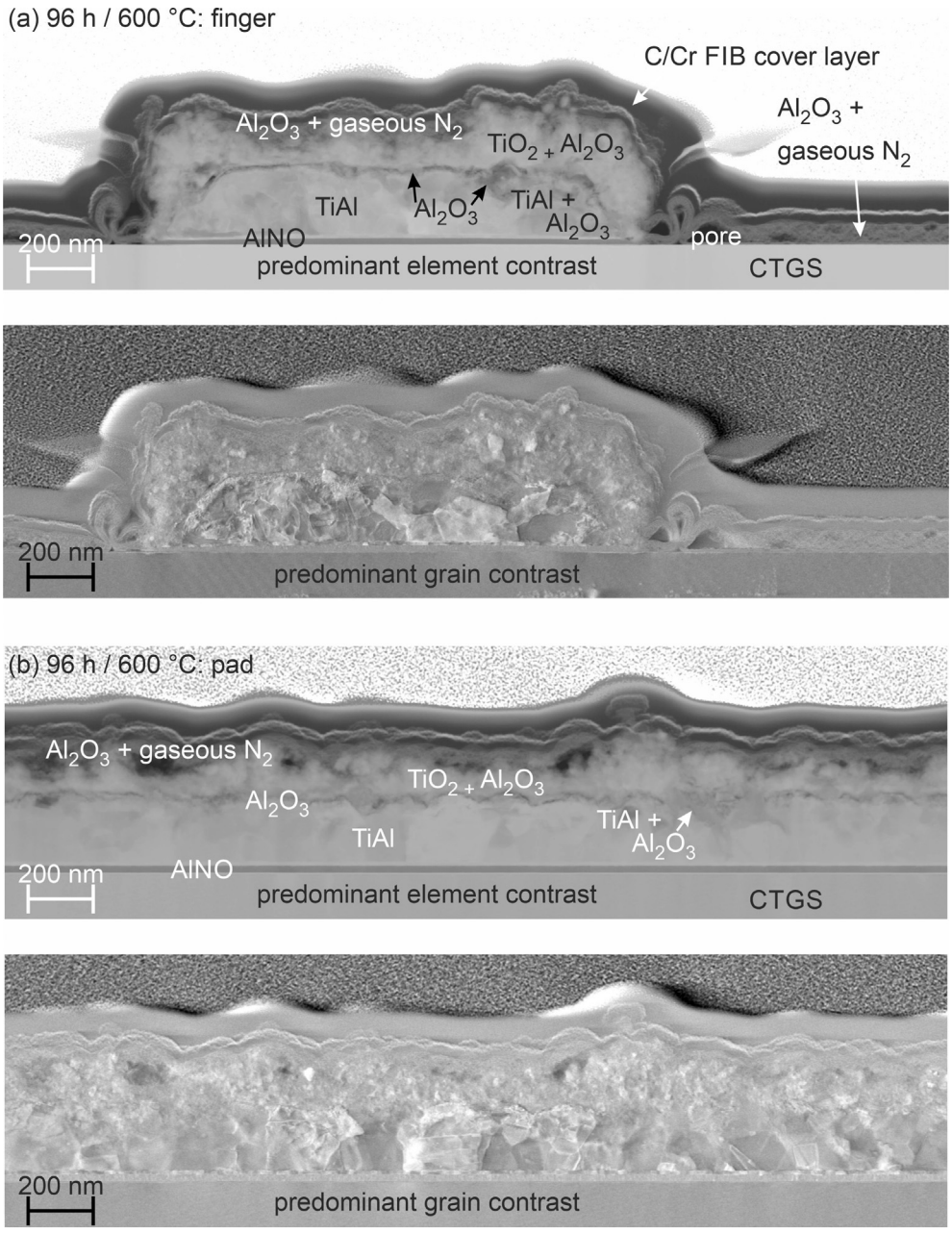

Figure A.5 – STEM images of the sample annealed for 96 h at 600 °C: (a) cross section of a finger electrode, (b) cross section of the contact pad. The top image shows predominant element contrast, the lower image shows predominant grain contrast.

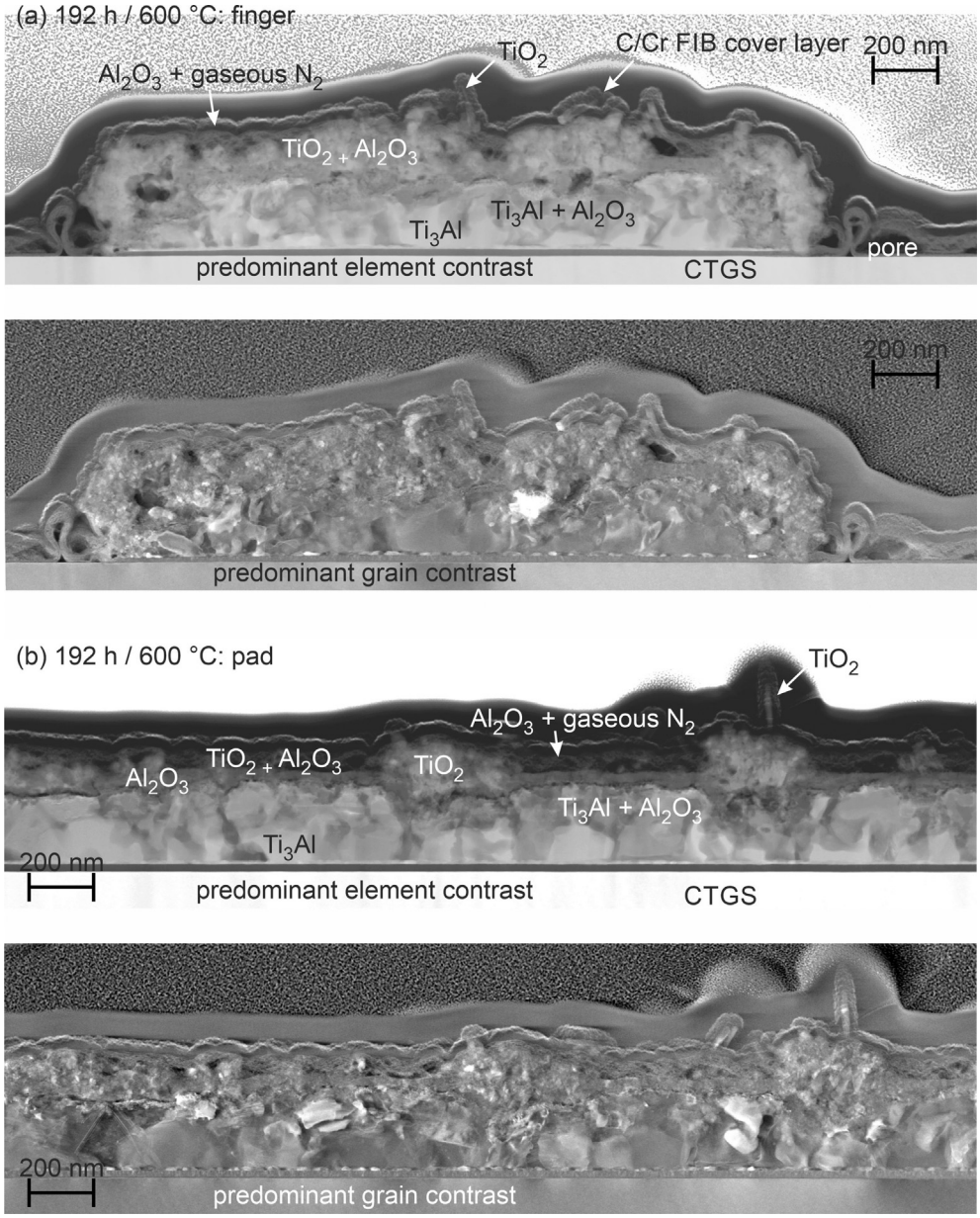

Figure A.6 – STEM images of the sample annealed for 192 h at 600 °C: (a) cross section of a finger electrode, (b) cross section of the contact pad. The top image shows predominant element contrast, the lower image shows predominant grain contrast.

REFERENCES

[1] Fritze H. High-temperature piezoelectric crystals and devices. J Electroceram 2011;26(1–4):122–61.
[2] Bruckner G, Bardong J. Wireless readout of multiple SAW temperature sensors. Sensors 2019;19(14):3077.
[3] Mandal D, Banerjee S. Surface acoustic wave (SAW) sensors: physics, materials, and applications. Sensors 2022;22(3):820.
[4] Elmazria O, Aubert T. Wireless SAW sensor for high temperature applications: material point of view. SPIE; 2011. p. 8066.
[5] Greve DW, Chin TL, Zheng P, Ohodnicki P, Baltrus J, Oppenheim IJ. Surface acoustic wave devices for harsh environment wireless sensing. Sensors 2013;13(6):6910–35.
[6] Aubert T, Elmazria O, Assouar B, Bouvot L, Hehn M, Weber S, et al. Behavior of platinum/tantalum as interdigital transducers for SAW devices in high-temperature environments. In: IEEE trans. Ultrason., ferroelect., freq. Contr. vol. 58; 2011. p. 603–10. 3.
[7] François B, Sakharov S, Droit C, Davis Z, Richter D, Fritze H, et al. Wireless temperature measurements above 500 °C using surface acoustic wave sensors. Procedia Eng 2012;47:1227–30.
[8] Liu X, Peng B, Zhang W, Zhu J, Liu X, Wei M. Improvement of high-temperature stability of Al_2O_3/Pt/ZnO/Al_2O_3 film electrode for SAW devices by using Al_2O_3 barrier layer. Materials 2017;10(12):1377.
[9] Weng H, Duan FL, Zhang Y, Hu M. High temperature SAW sensors on LiNbO3 substrate with SiO_2 passivation layer. IEEE Sensor J 2019;19(24):11814–8.
[10] Zhou X, Tan Q, Liang X, Li B, Guo T, Gan Y. Novel multilayer SAW temperature sensor for ultra-high temperature environments. Micromachines 2021;12(6):643.
[11] Moulzolf SC, Frankel DJ, da Cunha MP, Lad RJ. High temperature stability of electrically conductive Pt–Rh/ZrO_2 and Pt–Rh/HfO_2 nanocomposite thin film electrodes. Microsyst Technol 2014;20(4–5):523–31.
[12] Thiele JA, da Cunha MP. Platinum and palladium high-temperature transducers on langasite. In: IEEE trans. Ultrason., ferroelect., freq. Contr. vol. 52; 2005. p. 545–9. 4.
[13] Aubert T, Bardong J, Elmazria O, Bruckner G, Assouar B. Iridium interdigital transducers for high-temperature surface acoustic wave applications. IEEE Trans Ultrason Ferroelectrics Freq Control 2012;59(2):194–7.
[14] Sakharov S, Zabelin A, Medvedev A, Buzanov O, Kondratiev S, Roshchupkin D, et al. Technological process and resonator design optimization of Ir/LGS high temperature SAW devices. In: Proc. IEEE ultrasonics symposium 2014; 2014. p. 1632–5.
[15] Taguett A, Aubert T, Elmazria O, Bartoli F, Lomello M, Hehn M, et al. Comparison between Ir, $Ir_{0.85}Rh_{0.15}$ and $Ir_{0.7}Rh_{0.3}$ thin films as electrodes for surface acoustic waves applications above 800 °C in air atmosphere. Sensor Actuator Phys 2017;266:211–8.
[16] Rane GK, Seifert M, Menzel S, Gemming T, Eckert J. Tungsten as a chemically-stable electrode material on Ga-containing piezoelectric substrates langasite and catangasite for high-temperature SAW devices. Materials 2016;9(2):101.
[17] Menzel SB, Seifert M, Priyadarshi A, Rane GK, Park E, Oswald S, et al. Mo-La_2O_3 multilayer metallization systems for high temperature surface acoustic wave sensor devices. Materials 2019;12(17):2651.
[18] da Cunha MP, Lad R, Moonlight T, Bernhardt G, Frankel D. High temperature stability of langasite surface acoustic wave devices. Ultrason Symp 2008:205–8.
[19] Hofmann M, Gemming T, Wetzig K. Microstructure and composition of annealed Al/Ti-metallization layers. Anal Bioanal Chem 2004;379(4):547–53.
[20] Nüssl R, Jewula T, Ruile W, Sulima T, Hansch W. Correlation between texture and mechanical stress durability of thin aluminum films. Thin Solid Films 2014;556:376–80.
[21] Turnow H, Wendrock H, Menzel S, Gemming T, Eckert J. Structure and properties of sputter deposited crystalline and amorphous Cu–Ti films. Thin Solid Films 2016;598:184–8.
[22] Li Q, Fu S, Lu Z, Qian L, Wang R, Chen T, et al. Behavior of Al/Cu/Ti electrodes in surface acoustic wave filter at high power. Curr Appl Phys 2019;19(4):363–9.
[23] Lu Z, Fu S, Chen Z, Shen J, Su R, Wang R, et al. High-frequency and high-temperature stable surface acoustic wave devices on ZnO/SiO_2/SiC structure. J Phys D Appl Phys 2020;53(30):305102.
[24] Gao X, Cheng L, Xue X, Zhai S, Liang Y, Wang W, et al. Development of wireless and passive SAW temperature sensor with very high accuracy. Appl Sci 2021;11(16):7422.
[25] Seifert M, Lattner E, Menzel SB, Oswald S, Gemming T. Phase formation and high-temperature stability of very thin Co-sputtered Ti-Al and multilayered Ti/Al films on thermally oxidized Si substrates. Materials 2020;13(9):2039.
[26] Seifert M, Lattner E, Menzel S, Oswald S, Gemming T. Study of TiAl thin films on piezoelectric CTGS substrates as an alternative metallization system for high-temperature SAW devices. J Mat Res Technol 2021;12:2383–95.
[27] Seifert M. High temperature behavior of RuAl thin films on piezoelectric CTGS and LGS substrates. Materials 2020;13(7):1605.
[28] Seifert M, Brachmann E, Rane GK, Menzel SB, Oswald S, Gemming T. Pt-RuAl bilayers as a model system for Pt wire bonding of high-temperature RuAl electrodes. J Alloys Compd 2020;813:152107.
[29] Wang H, Reed RC, Gebelin JC, Warnken N. On the modelling of the point defects in the ordered B2 phase of the Ti–Al system: combining CALPHAD with first-principles calculations. Calphad 2012;39:21–6.
[30] Taniguchi S, Shibata T, Itoh S. Oxidation behavior of TiAl at high temperatures in purified oxygen. Mater Trans, JIM 1991;32(2):151–6.
[31] Kekare SA, Aswath PB. Oxidation of TiAl based intermetallics. J Mater Sci 1997;32(9):2485–99.
[32] Rahmel A, Spencer PJ. Thermodynamic aspects of TiAl and $TiSi_2$ oxidation: the Al-Ti-O and Si-Ti-O Phase diagrams. Oxid Metals 1991;35(1):53–68.